Anisotropic conductivity of uncharged domain walls in BiFeO₃

Anna N. Morozovska,[1] Rama K. Vasudevan,[2] Peter Maksymovych,[3] Sergei V. Kalinin,[3,*] and Eugene A. Eliseev[4,†]

[1]*Institute of Physics, National Academy of Sciences of Ukraine, 46, pr. Nauki, 03028 Kiev, Ukraine*
[2]*School of Materials Science and Engineering, University of New South Wales, Kensington, Sydney 2052, Australia*
[3]*Center for Nanophase Materials Science, Oak Ridge National Laboratory, Oak Ridge, Tennessee, 37831, USA*
[4]*Institute for Problems of Materials Science, National Academy of Sciences of Ukraine, 3, Krjijanovskogo, 03142 Kiev, Ukraine*
(Received 7 June 2012; published 20 August 2012)

Experimental observations suggest that nominally uncharged, as-grown domain walls in ferroelectrics can be conductive, yet comprehensive theoretical models to explain this behavior are lacking. Here, Landau-Ginzburg-Devonshire theory is used to evolve an analytical treatment of the anisotropic carrier accumulation by nominally uncharged domain walls in multiferroic BiFeO₃. Strong angular dependence of the carrier accumulation by 180° domain walls originates from local band bending via angle-dependent electrostriction and flexoelectric coupling mechanisms. Theoretical results are in qualitative agreement with experimental data and provide a counterpart that is consistent with recent first-principles calculations. These studies suggest that a significantly more diverse range of domain wall structures could possess novel electronic properties than previously believed. Similarly, emergent electronic behaviors at ferroic walls are typically underpinned by multiple mechanisms, necessitating first-principles studies of corresponding coupling parameters.

PACS number(s): 77.80.Dj, 77.80.bn, 73.40.−c

I. INTRODUCTION

Functionality of condensed matter systems are often controlled by small local distortions from ideal structure traditionally described through order parameters, which can represent any of several energetically degenerate ground states. In this description, regions with the same order parameter values (named, domains) are separated by the "walls", classified as topological defects,[1] which possess different symmetry and can display markedly different and new properties not exhibited in the bulk material.[2,3] Examples include ferroelectric, ferroelastic, and magnetic domain walls in ferroic materials, as well as ferromagnetic Mott insulators[4] and more subtle distortions such as Jahn-Teller walls.[5] From a technological perspective, ferroelectric and ferroelastic domain walls have been a foci of interest due to strong coupling with lattice strain and, correspondingly, significant strain-mediated effects such as polarization rotations[6] and ferroelastic phase transitions at the interface.[7] Additionally, the discovery of novel electronic properties arising at these domain walls has catalyzed significant experimental and theoretical interest in this topic.[5–9]

It has been known for decades that the existence of charged domain walls in ferroelectric semiconductors should result in free carriers accumulation or inversion in the vicinity of the domain wall and, thus, can lead to enhanced conductivity at the wall.[10] Remarkably, experimental verification of this prediction occurred only recently, by Seidel *et al.*, who used scanning probe microscopy (SPM) methods to report room-temperature metallic conductivity of 180° and 109° domain walls in BiFeO₃.[11,12] The authors found that the 71° domain walls did not exhibit conductivity. However, recent investigations of nominally uncharged fabricated vortex structures in BFO show an order-of-magnitude increase in conductivity over single domain regions.[13] Other experiments have shown that nominally uncharged as-grown 71° domain walls can also exhibit enhanced conductivity.[14] Farokhipoor *et al.*[14] reported that the conductivity at the domain walls in thin (40- to 70-nm) BFO films was similar for the 71° and 109° as-grown

domain walls, suggesting strain-related effects, as opposed to bound charge at the domain wall, are an important (yet poorly understood) factor in determining local electronic properties.

A. Domain wall conductance in BiFeO₃

Ferroelectric bismuth ferrite, BiFeO₃ (BFO), is the one of the most promising multiferroics due to giant spontaneous polarization (about 0.9 C/m² at room temperature), high ferroelectric Curie temperature (∼1100 K), strong antiferromagnetism (magnetic Curie temperature ∼650 K), and pronounced structural ordering (oxygen octahedron tilt).[15] Distorted perovskite-structured BiFeO₃ also exhibits intriguing physical properties, which most probably originate from the complex interplay between coexisting structural, polar, and magnetic ordering in the single domain regions and especially at the domain walls,[15,16] where the electronic properties can changes drastically.[11–14]

To illustrate the variability of the conductivity response at BiFeO₃ domain walls, experimental studies with current-atomic force microscopy (c-AFM) and piezoresponse force microscopy (PFM) of a 200-nm BFO film grown on a DyScO₃ substrate are shown in Fig. 1. The film consists of a 71° in-plane striped domain structure, with a domain spacing of ∼200 nm.[17] To form the other two types of domain walls, a square area was poled with the tip held at a voltage of −6 V. This results in both ferroelectric (180°) and ferroelastic (71°) switching, as shown by the vertical and lateral PFM phase images placed as shown in the insets in Fig. 1(a). The c-AFM image, taken with the tip held at voltage $V = -2.6$ V, shown in Fig. 1(a) (central image), indicates that conduction can be observed at all three types of domain walls. A close-up of the top-left quadrant is shown in Fig. 1(b), where a conducting 180° wall segment can be seen. Additionally, ultrahigh vacuum (UHV) SPM studies of the film, shown in the topography and c-AFM image in Figs. 1(c) and 1(d), indicate that as-grown 71° domain walls, which are nominally uncharged, are indeed conducting. Collectively, these experimental findings suggest that uncharged domain
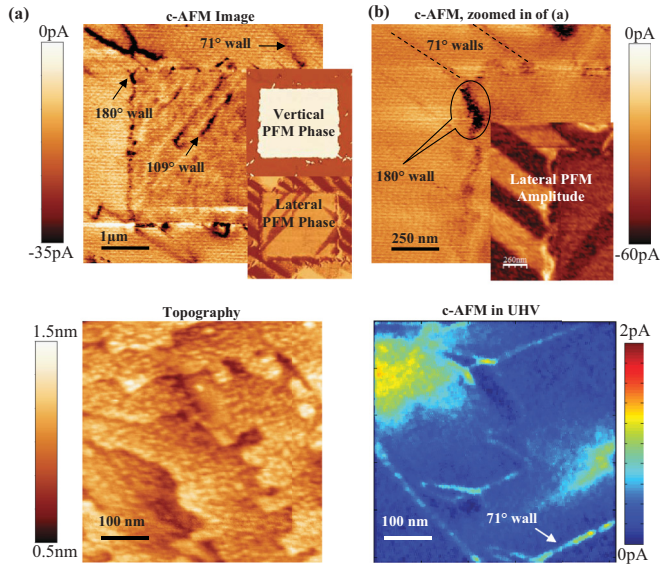
FIG. 1. (Color online) (a) c-AFM taken with $V_{\text{tip}} = -2.6$ V reveals that the 109° and 71° uncharged domain walls in BFO are conducting. The dark corner segment is a 180° wall, as indicated. Vertical and lateral PFM phase images are shown in the insets. (b) Close-up of (a), showing the conductive 180° wall segment, as well as 71° walls. Lateral PFM amplitude is shown in the inset. (c) Topography and (d) simultaneous c-AFM image, taken with $V_{\text{sample}} = +2$V, in the UHV of as-grown, conducting 71° domain walls.

walls and topological defects can exhibit electric conduction, seemingly at odds with existing theories as to the origins of the static domain wall's conductivity.

It is generally accepted that uncharged walls are thermodynamically stable and most energetically preferable in bulk ferroelectrics.[18] Consequently, the walls can be readily created in the required amount and their spatial location can be manipulated and controlled with nanoscale resolution by, e.g., SPM.[11–13] While the charge state of the domain walls in realistic systems is generally unknown, it is of interest to explore theoretically the electronic conductivity properties of uncharged walls at a prototypical ferroic wall.

The ferroelectric, structural, and magnetic properties of BiFeO$_3$ are relatively well studied both experimentally (see, e.g., Refs. 15 and 19) and theoretically (see, e.g., Ref. 20). Numerical *ab initio* calculations[21] and phase-field modeling based on phenomenological Landau theory[22] are available. Electronic properties of the domain walls, on the other hand, are much less studied. First-principles calculations of ferroelectric domain walls in BiFeO$_3$[21] showed that the band gap narrows on the values 0.2, 0.1, and 0.05 eV at nominally uncharged 180°, 109°, and 71° domain walls correspondingly. Despite this, an analytical Landau-type theory of the uncharged domain walls' conductivity in rhombohedral ferroelectrics is currently absent. It is worth noting that the Landau theory is a powerful method that, in 1969, was proven capable of predicting charged domain walls' static conductivity in ferroelectric semiconductors,[23] the conductivity mechanism stemming from compensation of polarization charge discontinuity by mobile carriers in the material. The analytical Landau-type theory was further developed for charged walls in uniaxial[24,25] and

multiaxial tetragonal ferroelectrics,[26] improper ferroelectrics,[2] and twin walls in incipient ferroelectrics–ferroelastics.[27] These studies agree with recent experiments on Pb(Zr,Ti)O$_3$,[28,29] ErMnO$_3$,[8] and LiNbO$_3$.[30]

The gap between experimental observations of conductivity at nominally uncharged walls and the existing theoretical frameworks, as well as the potential for use of such walls in technological applications ("domain wall nanoelectronics"[16]), motivate an analytical study of the free carrier accumulation by nominally uncharged 180°, 109°, and 71° domain walls in bulk BiFeO$_3$. Using Landau-Ginzburg-Devonshire (LGD) theory we show that polarization changes via flexoelectric coupling and inhomogeneous elastic strains give rise to strongly anisotropic local band bending and carrier accumulation by nominally uncharged domain walls. These results rationalize experimentally observed conductivity at nominally uncharged domain walls and further suggest that spatial modulation of conduction via secondary strain-related effects is possible even in the systems where charged domain walls are thermodynamically unstable.

II. BASIC EQUATIONS AND THEIR ANALYTICAL SOLUTION

Here the conductivity of uncharged domain walls in BiFeO$_3$ is explored. For rhombohedral materials, the three types of domain walls are 180°, 109°, and 71° walls, as shown in Figs. 2(a)–2(c), respectively.

A. Basic equations

Within LGD theory, the Gibbs free energy functional density written for the BiFeO$_3$ parent symmetry m3m has the form[26]

$$G = a_i P_i^2 + a_{ij} P_i^2 P_j^2 + a_{ijk} P_i^2 P_j^2 P_k^2 + \frac{g_{ijkl}}{2} \frac{\partial P_i}{\partial x_j} \frac{\partial P_k}{\partial x_l}$$
$$- Q_{ijkl} \sigma_{ij} P_k P_l + \frac{F_{ijkl}}{2} \left(\sigma_{ij} \frac{\partial P_k}{\partial x_l} - P_k \frac{\partial \sigma_{ij}}{\partial x_l} \right)$$
$$- \frac{s_{ijkl}}{2} \sigma_{ij} \sigma_{kl} - P_i E_i - \frac{\varepsilon_0 \varepsilon_b}{2} E_i^2 + \rho \varphi. \quad (1)$$

Subscripts 1, 2, and 3 denote Cartesian coordinates x, y, z; P_i is ferroelectric polarization components; a_i, a_{ij}, and a_{ijk} are LGD expansion coefficients of the second-, fourth-, and sixth-order dielectric stiffness tensors, correspondingly; gradient coefficients are g_{ijkl};[31] Q_{ijkl} are fourth rank electrostriction tensors coefficients; and F_{ijkm} are the flexoelectric strain tensor coefficients. σ_{ij} are elastic stresses and $\frac{s_{ijkl}}{2} \sigma_{ij} \sigma_{kl}$ is elastic energy, s_{ij} are elastic compliances. $E_k = -\partial \varphi / \partial x_k$ are the components of depolarization electric field, φ is the electric field potential, ε_b is background permittivity,[32] and $\varepsilon_0 = 8.85 \times 10^{-12}$ F/m is the dielectric constant of the vacuum. The space charge density is $\rho = e(N_d^+ - N_a^- + p - n)$, where $e = 1.6 \times 10^{-19}$ C is the electron charge, n is the electron density in the conduction band, p is hole density in the valence band, and N_d^+ and N_a^- are the concentrations of ionized donors and acceptors, correspondingly. Electrostatic potential φ should be determined from the Poisson equation $\varepsilon_0 \varepsilon_b \frac{\partial^2 \varphi}{\partial x_i^2} = \frac{\partial P_i}{\partial x_i} - \rho$.
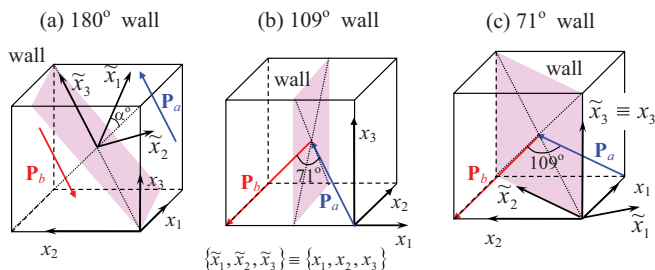
FIG. 2. (Color online) Rotated coordinate frame $\{\tilde{x}_1, \tilde{x}_2, \tilde{x}_3\}$ choice for (a) 180°, (b) 109°, and (c) 71° uncharged domain walls in a rhombohedral ferroelectric BiFeO$_3$. Pseudocubic crystallographic axes are $\{x_1, x_2, x_3\}$. Domain wall rotation angle α is counted from $\tilde{x}_3$ axis.

Regarding that all physical quantities can depend only on the distance $\tilde{x}_1$ from the domain wall plane $\tilde{x}_1 = 0$ (as shown in Figs. 2), it make sense to define them in the coordinate frame $\{\tilde{x}_1, \tilde{x}_2, \tilde{x}_3\}$ rotated with respect to the pseudocubic crystallographic axes $\{x_1, x_2, x_3\}$. The domain wall rotation angle α is counted from $\tilde{x}_3$ axes. To maintain charge neutrality, the rotation angle α can be arbitrary for 180° uncharged domain walls in the equilibrium, while $\alpha = 0, \pi$ for 109° and $\alpha = -\pi/4, 3\pi/4$ for 71° uncharged domain walls in rhombohedral material.

Euler-Lagrange equations[33] for polarization components were derived from the minimization of the Gibbs free energy functional as $\partial \tilde{G}/\partial \tilde{P}_i - \partial(\partial \tilde{G}/\partial(\partial \tilde{P}_i/\partial \tilde{x}_1))/\tilde{x}_1 = 0$; they are listed in Appendix S1.[34] Equations of state for elastic stresses are $\partial \tilde{G}/\partial \tilde{\sigma}_{ij} = -\tilde{u}_{ij}$, where $\tilde{u}_{ij}$ are elastic strains. They were solved along with mechanical equilibrium conditions $\partial \tilde{\sigma}_{1j}/\partial \tilde{x}_1 = 0$, compatibility relation $e_{i1l}e_{j1n}(\partial^2 \tilde{u}_{ln}/\partial \tilde{x}_1^2) = 0$, and boundary condition $\tilde{\sigma}_{ij}(\tilde{x}_1 \to \pm\infty) = 0$. Analytical expressions for elastic stresses are listed in Appendix S2.[34] After the substitution of the elastic stresses in the Euler-Lagrange equations, they become coupled and with the 1D-Poisson equation $\varepsilon_0 \varepsilon_b \partial^2 \varphi/\partial \tilde{x}_1^2 = \partial \tilde{P}_1/\partial \tilde{x}_1 - e\rho$. The boundary conditions to the Poisson and Euler-Lagrange and equations are $\varphi(\tilde{x}_1 \to \pm\infty) \to 0$, $\tilde{P}_3(\tilde{x}_1 = 0) = 0$, $\tilde{P}_3(\tilde{x}_1 \to +\infty) = +\tilde{P}_S$, and $\tilde{P}_{1,2}(\tilde{x}_1 \to \pm\infty) \to 0$.

B. Analytical solution

Analytical expressions for elastic strains variations δu_{ij} caused by uncharged domain walls have the form

$$\delta\tilde{u}_{22} = \delta\tilde{u}_{33} = \delta\tilde{u}_{23} = 0, \tag{2}$$

$$\delta\tilde{u}_{i1} = \sum_{j,k=1}^{3} \left(\vartheta_{ijk}\left(\tilde{P}_j\tilde{P}_k - \tilde{P}_j^S\tilde{P}_k^S\right) + \Psi_{ij}\frac{\partial\tilde{P}_j}{\partial\tilde{x}_1} \right). \tag{3}$$

Here $\delta\tilde{u}_{ij} = \tilde{u}_{ij} - \tilde{u}_{ij}^S$, where $\tilde{u}_{ij}^S$ is the spontaneous strain far from the wall. $\tilde{P}_i^S$ are spontaneous polarization components, which depend on the wall type. Coefficients ϑ_{ijk} in Eq. (3) are proportional to the combinations of the electrostriction tensors' coefficients Q_{ij} and $\tilde{Q}_{ij}$, and the elastic compliances s_{ij} and $\tilde{s}_{ij}$are defined in the crystallographic $\{x_1, x_2, x_3\}$ and rotated $\{\tilde{x}_1, \tilde{x}_2, \tilde{x}_3\}$ frames correspondingly. Coefficients Ψ_{ij} are proportional to the flexoelectric coupling coefficients F_{ij} and $\tilde{F}_{ij}$, s_{ij} and $\tilde{s}_{ij}$. The coefficients and rotated tensors'

components are listed in Table S1a[34] for uncharged 180° domain walls and in Table S1b for uncharged 109° and 71° domain walls.

Polarization components $\tilde{P}_i$ can be calculated numerically from the system of coupled Euler-Lagrange equations allowing for electrostriction, flexoelectric coupling, and the depolarization field $\tilde{E}_1$ acting on the component $\tilde{P}_1$ (see details in Ref. 26). Due to the smallness of the flexoelectric coupling, it appeared possible to use a perturbation approach[35] in order to derive analytical expressions for $\tilde{P}_i$ in the considered domain wall geometries. The corresponding expressions are listed in Table S2.[34]

For all types of walls, we use the Ising component $\tilde{P}_3^S \approx \tilde{P}_3^S \tanh(\tilde{x}_1/L_c)$, where the function $\tanh(\tilde{x}_1/L_c)$ should be used for the materials with a second-order ferroelectric phase transition, like BiFeO$_3$. Correlation length L_c also depends on the wall type and is listed in Table S2.[34] The polarization variation $\delta\tilde{P}_3(\tilde{x}_1)$ was omitted as proportional to the second powers of the flexoelectric coupling coefficient.

The polarization variations $\delta\tilde{P}_i = \tilde{P}_i - \tilde{P}_i^S$ ($i = 1,2$) originate from the flexoelectric [term $\sim f_i^Q(\partial\tilde{P}_3^2/\partial\tilde{x}_1)$] and the purely electrostriction [term $\sim q_i\tilde{P}_3((\tilde{P}_3^S)^2 - \tilde{P}_3^2)$] couplings, and $\tilde{P}_{1,2}^S \equiv 0$ for a 180° wall. The expressions for f_i^Q and q_i are listed at the end of Table S2.[34] Linear variations $\delta\tilde{P}_2$ are absent for 109° and 71° uncharged domain walls, since $f_2^Q(\alpha) \sim \sin(4\alpha)$ and $q_2(\alpha) \sim \sin(4\alpha)$ are zero for the corresponding angles $\alpha = 0, \pi, -\pi/4, 3\pi/4$.

Approximate analytical expression for Bloch-type component in the vicinity of 180° wall

$$\tilde{P}_2 \approx P_b \cosh^{-2}\left(\frac{\tilde{x}_1}{L_c}\right) + \frac{f_2^Q}{2\beta}\frac{\partial\tilde{P}_3^2}{\partial\tilde{x}_1} + \frac{q_2}{2\beta}\tilde{P}_3\left(\left(\tilde{P}_3^S\right)^2 - \tilde{P}_3^2\right) \tag{4}$$

gives an overestimated value that does not account for gradient effects. A more rigorous expression, including this effect, was derived by Yudin *et al.*[36] for the case of tetragonal BaTiO$_3$. Note that Bloch-type walls were calculated previously in rhombohedral BaTiO$_3$ at low temperatures[37] and tetragonal PbTiO$_3$[38] without consideration of the flexoelectric coupling. Therefore, it is assumed that a nonzero Bloch component $\tilde{P}_2 = P_b \cosh^{-2}(\tilde{x}_1/L_c)$ is possible in the rhombohedral phase of BiFeO$_3$. The solution is unrelated with flexoelectric coupling and is symmetric with respect to $\tilde{x}_1$, i.e., it has even $\tilde{x}_1$ parity. Since no compact analytical expression for P_b can be derived, its existence was studied numerically. Numerical simulations showed that the even $\tilde{x}_1$-parity Bloch solution can appear at angles $\alpha = m\pi/3 + \pi/2$ (m is integer), corresponding to the absence of the odd $\tilde{x}_1$-parity terms in Eq. (4), since $f_2^Q = q_2 = 0$ at these angles simultaneously. However, the even $\tilde{x}_1$-parity seeding is required for the even-parity Bloch component origin, while the amplitude P_b is seeding independent. So the appearance of the even solution, as the typical manifestation of the spontaneous symmetry breaking across the wall, should be essentially energetically preferable in order to be dominant. Estimations of the corresponding wall energies proved that the even $\tilde{x}_1$-parity solution gives no more than a several-percentages energy gain in comparison with the odd-type solution at angles $\alpha = m\pi/3 + \pi/2$. Meanwhile,

the odd $\tilde{x}_1$-parity solution is induced by "seeding" that is proportional to f_2^Q and q_2 and is energetically preferable at the angles $\alpha \neq m\pi/3 + \pi/2$. Moreover, the even $\tilde{x}_1$-parity Bloch solution energy and features appeared to be strongly dependent on the gradient tensor g_{ij} values and anisotropy. Since the exact values and anisotropy of the gradient tensor is unknown for BiFeO$_3$, and below $P_b = 0$ is substituted, the question regarding the interplay of the odd-parity and even-parity Bloch solutions is left for future study.

The expression for the Neel-type component

$$\tilde{P}_1 \approx \frac{\varepsilon_0 \varepsilon_b f_1^Q}{1 + 2\beta\varepsilon_0\varepsilon_b} \frac{\partial \tilde{P}_3^2}{\partial \tilde{x}_1} + \frac{\varepsilon_0 \varepsilon_b q_1 \tilde{P}_3}{1 + 2\beta\varepsilon_0\varepsilon_b}\left(\left(\tilde{P}_3^S\right)^2 - \tilde{P}_3^2\right) \quad (5)$$

appeared to be rather accurate in the vicinity of 180° wall. Here the first term has a flexoelectric nature and the second term originates from electrostriction coupling via the constant $\beta \approx a_1 + (\tilde{a}_{13} + \tilde{Q}_{44}^2/2\tilde{s}_{44})\tilde{P}_S^2$. Note that $\tilde{P}_1$ is nonzero for all angles α, except $\alpha = m\pi/3$. The result implies that the *nominally* uncharged 180° wall cannot be regarded to be completely uncharged in BiFeO$_3$, since the bound charge appears from the Neel component $\tilde{P}_1$. The latter can be rather small but (as will be shown below) enough to induce carrier accumulation.

The Neel component $\tilde{P}_1$ creates the "bare" depolarization field $\tilde{E}_1 \approx -\tilde{P}_1/\varepsilon_0\varepsilon_b$ that, in turn, strongly suppresses the component. The depolarization field leads to the electric potential variation

$$\varphi(\tilde{x}_1) \approx \frac{1}{1 + 2\beta\varepsilon_0\varepsilon_b}\left(f_1^Q + q_1 \frac{L_c \tilde{P}_3^S}{2}\right)\left(P_3^2(\tilde{x}_1) - \left(\tilde{P}_3^S\right)^2\right). \quad (6)$$

Since for many ferroelectrics $2\beta\varepsilon_0\varepsilon_b \ll 1$, the potential variation appeared almost independent on the product $\varepsilon_0\varepsilon_b$. The potential variation, in turn, changes the electrochemical potential variation in the vicinity of the domain wall.

The coupling between the inhomogeneous strain and band structure is given by the deformation potential.[39–42] The strain-induced conduction and valence band edge shift caused by the domain wall is linearly proportional to the strain variation $\delta\tilde{u}_{ij}$,[43]

$$E_{C,V} = E_{C0,V0} + \tilde{\Xi}_{ij}^{C,V}\delta\tilde{u}_{ij}, \quad (7)$$

where E_C and E_V are the energetic positions of the bottom of the conduction band and the top of the valence band, respectively, and $\tilde{\Xi}_{ij}^{C,V}$ is a tensor deformation potential of electrons in the conduction (C) or valence (V) bands. Values $E_{C0} = E_C(\tilde{u}_{ij}^S)$ and $E_{V0} = E_V(\tilde{u}_{ij}^S)$ already include the spontaneous strain $\tilde{u}_{ij}^S$ that exists far from the domain wall. The symmetry of the deformation potential tensors $\tilde{\Xi}_{ij}^{C,V}$ in the Γ point is determined by the crystal spatial symmetry.[43] In particular, the components $\Xi_{11}^{C,V} = \Xi_{22}^{C,V} = \Xi_{33}^{C,V}$ should be equal and nonzero in the rhombohedral phase of the bulk ferroelectric BiFeO$_3$.

The band edge shift [Eq. (7)], induced by the inhomogeneous strains [Eq. (3)] via the deformation potential, and electric potential variation [Eq. (6)] modulate the densities of the free electrons and holes accumulated by the domain wall.

The effect can be estimated in the Boltzmann approximation as[44]

$$f(\tilde{x}_1) \approx f_0 \exp\left(\frac{\Delta E_f(\tilde{x}_1)}{k_B T}\right). \quad (8)$$

The value $f = n$ for free electrons or $f = p$ for holes correspondingly; n_0 and p_0 are their equilibrium densities; $k_B = 1.3807 \times 10^{-23}$ J/K, and T is the absolute temperature. Local band bending ΔE_f are introduced as

$$\Delta E_f(\tilde{x}_1) = \mp\Xi_{ij}^f\delta\tilde{u}_{ij}(\tilde{x}_1) \pm e\varphi(\tilde{x}_1). \quad (9)$$

The upper signs correspond to the electrons ($f = n$), and the bottom signs correspond to the holes ($f = p$). Allowing for the possible Fermi level strain dependence,[45] $E_F(\tilde{u}_{ij}) = E_{F0}(\tilde{u}_{ij}^S) + \tilde{\xi}_{ij}^F\delta\tilde{u}_{ij}$, the "effective" deformation potentials are introduced in Eq. (9) as

$$\Xi_{ij}^f = \tilde{\Xi}_{ij}^{C,V} - \tilde{\xi}_{ij}^F. \quad (10)$$

The exact strain dependence of ΔE_f is unknown for BiFeO$_3$, where the band structure is extremely complex and degenerated, and improper conductivity is typically of mixed p type.[46] Hence, below we explore both cases in Eq. (9) (the case $\Xi_{ij}^f = 0$ in comparison with $\Xi_{ij}^f \neq 0$), since estimations for the band-gap derivative $\partial E_g/\partial u_{ij} \sim 20$ eV are available.[47] For a diagonal effective deformation potential tensor considered hereinafter, the convolution $\tilde{\Xi}_{ij}^f\delta\tilde{u}_{ij}$ gives $\Xi_{11}^f\delta\tilde{u}_{11}$, allowing for Eq. (3).

Equations (8) and (9) allow one to estimate quantitatively the relative contributions of the deformation potential, electrostriction, and flexoelectric coupling in the band bending, carrier density variation, and static conductivity across uncharged domain walls. Electrostriction coefficients and elastic compliances are relatively well known for typical ferroelectrics (see Table S3[34]). Numerical values of the deformation potential tensor components are poorly known for ferroelectrics. Below the estimation $|\Xi_{ij}^{C,V}| \sim (5$–$20)$ eV is used, consistent with experimental result for BiFeO$_3$[47] and *ab initio* calculations for SrTiO$_3$.[48] Flexoelectric coefficient values F_{ij} can be estimated as $\sim 10^{-11}$ C^{-1} m^3 from experiment for SrTiO$_3$[49] and vary in the range $(1$–$100) \times 10^{-11}$ C^{-1} m^3 for BaTiO$_3$[50] and $F_{ij} \sim 300 \times 10^{-11}$ C^{-1} m^3 for PbZr$_{0.2}$Ti$_{0.8}$O$_3$.[51] The Kogan microscopic model[52] gives $F_{ij} \sim 10^{-11}$ C^{-1} m^3 for all perovskites with lattice constant 0.4 nm. For BiFeO$_3$ with parent m3m symmetry, the nonzero components of the flexoelectric tensor are F_{11}, F_{12}, and F_{44}.

Using the estimations for Ξ_{ij}^p and F_{ij}, and BiFeO$_3$ parameters from Table S3,[34] in the next section we show that the contributions of the flexoelectric coupling and deformation potential in the uncharged domain wall conductivity are comparable and can lead to an increase of the wall static conductivity that ranges from one to three orders of magnitude.

III. CARRIER ACCUMULATION BY FLAT WALLS

The anisotropic nature of the carriers accumulation by uncharged 180° domain walls follows from the strong dependence of the flexoelectric and electrostriction coefficients on the wall rotation angle α. Angular dependencies of the local band bending and hole density accumulated by 180° domain
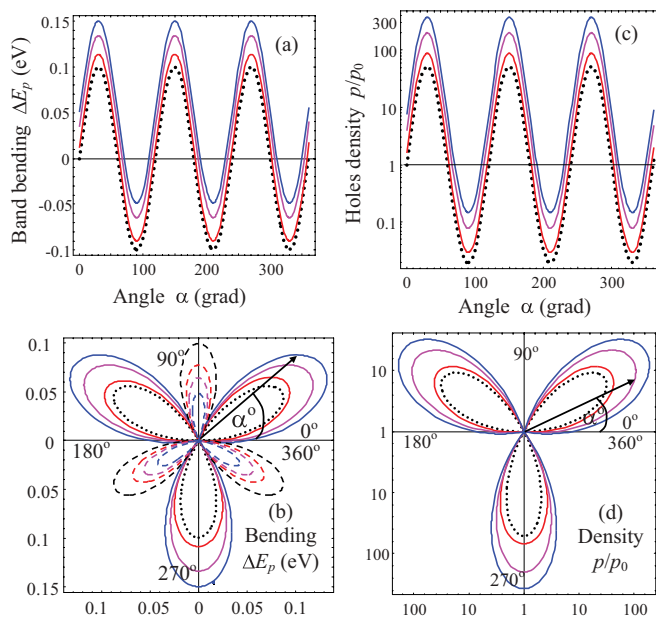
FIG. 3. (Color online) Anisotropic local band bending $\Delta E_p(0)$ [(a) and (b)] and holes density $p(0)/p_0$ [(c) and (d)] angular dependencies caused by nominally uncharged 180° domain walls in rhombohedral multiferroic BiFeO$_3$ at room temperature, 293 K. Black dotted curves are calculated without deformation potential $\Xi_{ij}^p = 0$ and flexoelectric coupling $F_{ij} = 0$. Solid curves are calculated for different coefficients: $F_{11} = -1.38 \times 10^{-11}$ C^{-1} m^3, $F_{12} = 0.67 \times 10^{-11}$ C^{-1} m^3, $F_{44} = 0.85 \times 10^{-11}$ C^{-1} m^3 and $\Xi_{ij}^p = 0$ (red solid curves); $2F_{ij}$ and $\Xi_{ij}^p = 21$ eV (magenta solid curves); $3F_{ij}$ and $\Xi_{ij}^p = 21$ eV (blue solid curves). Dashed curves in the polar plot (c) correspond to the negative $\Delta E_p(\tilde{x}_1)$. BiFeO$_3$ parameters are listed in Table S3.[34]

walls in p-type BiFeO$_3$ are shown in Fig. 3 for different values of flexoelectric coupling coefficients F_{ij} and deformation potential Ξ_{ij}^p. For the case $\Xi_{ij}^p = 0$ and $F_{ij} = 0$ (dotted curves), a strong anisotropy originates from the angular dependence of the electrostriction coefficients. The corresponding band bending angular dependence is quasiharmonic, $\Delta E_p(\tilde{x}_1 = 0) \sim E_0 \sin(3\alpha)$. One can see from Fig. 3(a) that flexoelectric coupling shifts the angular dependence as $\Delta E_p(\tilde{x}_1 = 0) \sim E_0 \sin(3\alpha) + \delta E$, where the shift δE is proportional to the coupling strength F_{ij}. Band bending and hole density are minimal at the angles $\alpha = 3\pi/6, 7\pi/6, 11\pi/6$ and maximal at the angles $\alpha = \pi/6, 5\pi/6, 9\pi/6$. Bulk level $\Delta E_p = 0$ and $p = p_0$ correspond to the angles $\alpha = 0, \pi/3, 2\pi/3$ at $F_{ij} = 0$ and weakly shift the F_{ij} increase. Modulation depth of the carriers accumulation/depletion is about one to two orders of magnitude depending on the F_{ij} values. In particular, the hole density at the wall can increase by a factor of 50 in comparison with a bulk value at $\Xi_{ij}^p = 0$ and $F_{ij} = 0$ and by a factor of 100 for realistic values of the flexoelectric coefficients $F_{11} = -1.38 \times 10^{-11}$ C^{-1} m^3, $F_{12} = 0.67 \times 10^{-11}$ C^{-1} m^3, $F_{44} = 0.85 \times 10^{-11}$ C^{-1} m^3 corresponding to SrTiO$_3$[49] and the effective deformation potential $\Xi_{ij}^p = 21$ eV estimated for BiFeO$_3$ from experiment.[47] The accumulation effect appeared relatively insensitive to the deformation potential value (compare dotted black curves for $\Xi_{ij}^p = 0$ with red curves for $\Xi_{ij}^p = 21$ eV). The polar plot in Fig. 3(c) demonstrates a

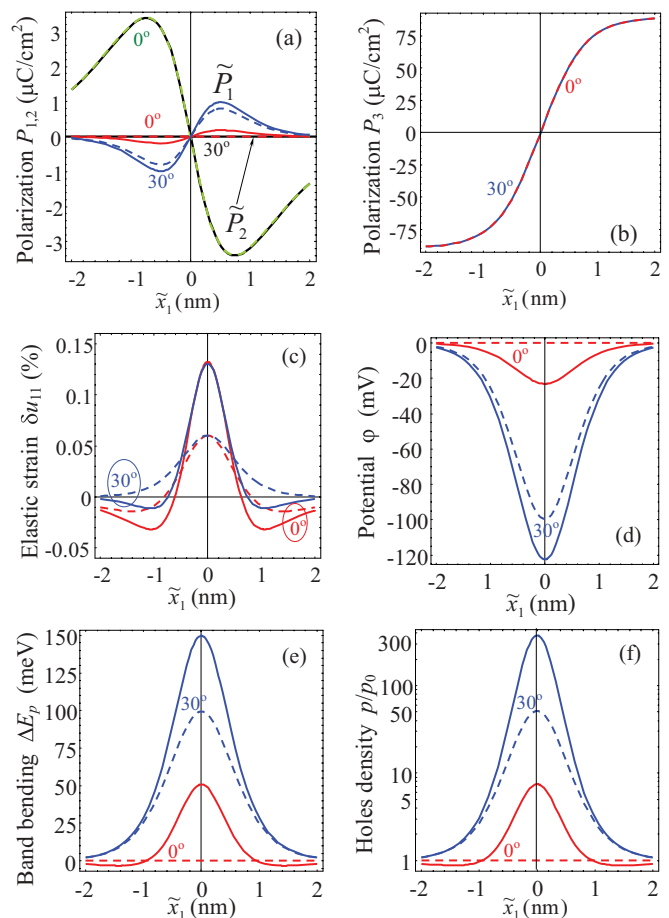FIG. 4. (Color online) $\tilde{x}_1$ profiles of polarization components $\tilde{P}_1$ (a), $\tilde{P}_2$ (a), and $\tilde{P}_3$ (b); the elastic strain variation $\delta\tilde{u}_{11}$ (c); potential variation φ (d); band bending ΔE_p (e); and carrier density p/p_0 (f) calculated across nominally uncharged 180° domain walls in rhombohedral BiFeO$_3$ for flexoelectric coupling coefficients $F_{11} = -4.14 \times 10^{-11}$ C^{-1} m^3, $F_{12} = 2.01 \times 10^{-11}$ C^{-1} m^3, $F_{44} = 2.55 \times 10^{-11}$ C^{-1} m^3 and deformation potential $\Xi_{ij}^p = 21$ eV (solid curves) and for $\Xi_{ij}^p = 0$ and $F_{ij} = 0$ (dashed curves). Rotation angle $\alpha = 0°$, 30° (labels near the curves), $T = 293$ K.

six-lobe structure, where three longer lobes (solid curves) correspond to the positive band bending ΔE_p and three smaller lobes (dashed curves) correspond to the negative ΔE_p. The difference between sizes of "positive" and "negative" lobes increases with the amplitude of the flexoelectric coupling increase. The polar plot in Fig. 3(d) demonstrates a three-lobe structure, where each lobe corresponds to the accumulation of holes by the wall.

Polarization components, strain, potential, band bending, and hole density $\tilde{x}_1$ profiles across the 180° domain wall were calculated for $\Xi_{ij}^p = 0$ and $F_{ij} = 0$ (shown by the dashed curves in Fig. 4) and for $\Xi_{ij}^p = 21$ eV and $F_{11} = -4.14 \times 10^{-11}$ C^{-1} m^3, $F_{12} = 2.01 \times 10^{-11}$ C^{-1} m^3, $F_{44} = 2.55 \times 10^{-11}$ C^{-1} m^3 (shown by the solid curves in Fig. 4). The values F_{ij} are three times higher than the ones for SrTiO$_3$.[49] Wall rotation angle α varied in the angular range 0–30°; the range corresponds to one-half of the first lobe shown in Figs. 3(c) and 3(d). Figure 4(a) shows that the spatial distributions of $\tilde{P}_1$ and $\tilde{P}_2$ are antisymmetric with respect to

the wall plane $\tilde{x}_1 = 0$. For all cases, the $\tilde{P}_2$ value is at least 3 times higher than the $\tilde{P}_1$ one, since $\tilde{P}_2$ is not suppressed by the depolarization field $\tilde{E}_1$. The polarization component $\tilde{P}_1$ strongly depends on the angle α and the flexoelectric coupling strength. It is seen from the Fig. 4(b) that polarization component $\tilde{P}_3$ is almost independent on the angle α and flexoelectric coupling value as anticipated from Table S2. The strain $\delta\tilde{u}_{11}$ is dependent on the flexoelectric coupling, but its maximal value is almost independent on the angle α [compare solid and dashed curves in Fig. 4(c)]. Dependencies of potential φ on $\tilde{x}_1$ are bell shaped and symmetric with respect to the wall plane $\tilde{x}_1 = 0$ [see Fig. 4(d)]. The contribution of the potential term, $e\varphi$, into the band bending ΔE_p typically dominates over the strain contribution $\Xi_{11}^p \delta\tilde{u}_{11}$ [compare values and profiles shape in Figs. 4(c)–4(e)]. Therefore, rather strong (up to 50–300 times in comparison with the equilibrium value) the accumulation of the free carriers by the 180° wall is governed by the potential variation caused by the Neel component $\tilde{P}_1$ [Fig. 4(f)]. Overall, the flexoelectric coupling contribution induces and/or enhances the strain, potential variation, and band bending maximal values, but the shape of the corresponding $\tilde{x}_1$ profiles remains almost the same with the coupling strength increase (compare the dashed and solid curves in Figs. 4).

A detailed study of the carrier accumulation/depletion by the 71° and 109° uncharged domain walls in BiFeO$_3$ was performed in a way similar to that carried out for the 180° domain walls. Representative results are shown in Figs. 5. In contrast to the equilibrium 180° uncharged domain walls, where the rotation angle α can be arbitrary, it is not the case for

the 109° uncharged domain walls, where $\alpha = 0$ (or π), and for 71° domain walls, where $\alpha = -\pi/4$ (or $3\pi/4$) in equilibrium [compare Figs. 2(a) with 2(b) and 2(c)]. Maximum on the $\tilde{x}_1$ profiles of holes density are located at the 109° and 71° weakly charged domain walls [Figs. 5(a) and 5(d)]. In contrast to the 180° walls, the flexoelectric coupling decreases the hole accumulation effect for the 109° and 71° walls [compare solid and dashed curves in Figs. 5(b) and 5(c)]. This is because the potential variation $e\varphi$ has a positive sign across the walls [see Figs. 5(b) and 5(d)] and so counteracts the hole accumulation induced by the positive deformation potential term, $\Xi_{11}^p \delta\tilde{u}_{11}$, since $\delta\tilde{u}_{11} > 0$, as one can see from Figs. 5(c) and 5(e). The resulting band bending, $\Delta E_p = \Xi_{11}^p \delta\tilde{u}_{11} - e\varphi$, becomes smaller than the value $\Xi_{11}^p \delta\tilde{u}_{11}$ calculated without flexoelectric coupling, since $\varphi \equiv 0$ for $F_{ij} = 0$ [compare the solid and dashed curves in Figs. 5(b) and 5(d)]. The width of potential and strain maxima is about 1 nm. Thus, the charging of the nominally uncharged walls originates from the flexoelectric coupling that induces Neel component of polarization, $\tilde{P}_1$, which, in turn, induces a corresponding depolarization field and potential variation.

Theoretical results presented in Figs. 3–5 are in good agreement with the first-principles studies[21] of ferroelectric domain walls in BiFeO$_3$, which showed that the band gap narrows on the value 0.2, 0.1, and 0.05 eV at uncharged 180°, 109°, and 71° domain walls correspondingly.

One of the simplest ways to verify experimentally our theoretical predictions for the 180° domain walls in BiFeO$_3$ is to study the conductivity on the cylindrical domain walls and its anisotropy. Cylindrical domains can be readily created
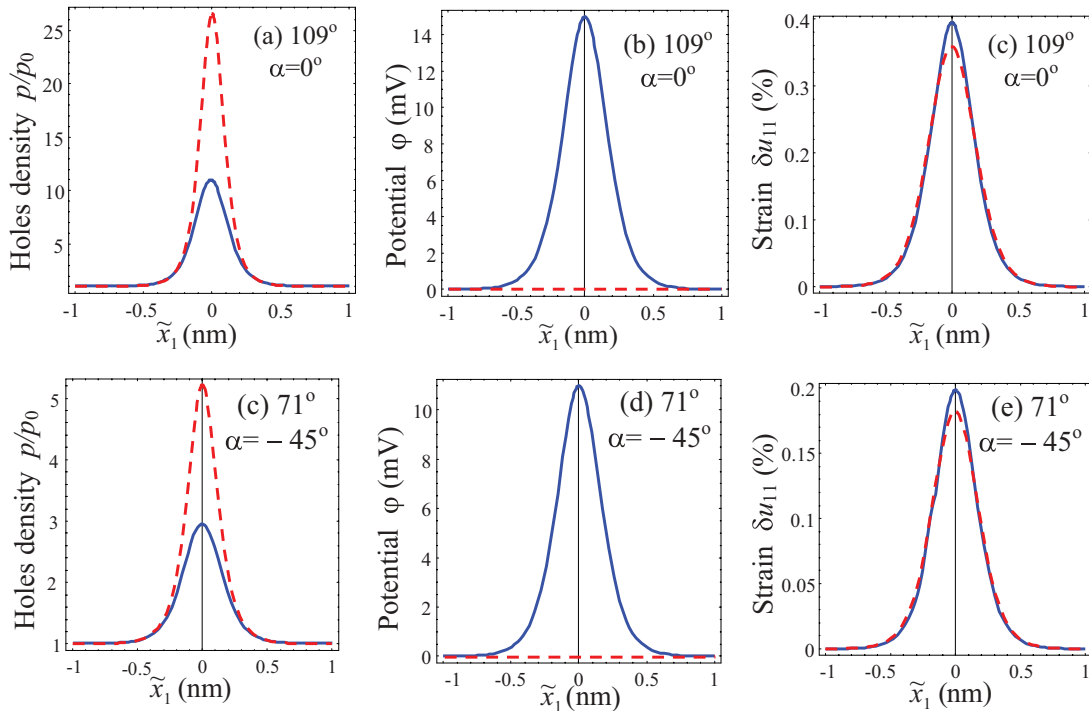

FIG. 5. (Color online) $\tilde{x}_1$ profiles of hole density p/p_0 [(a) and (c)], potential φ [(b) and (d)], and elastic strain $\delta\tilde{u}_{11}$ [(c) an (e)] variations across the 109° [(a) and (c)] and 71° [(d) an (f)] nominally uncharged domain walls. Blue solid profiles are calculated for flexoelectric coupling coefficients $F_{11} = -1.38 \times 10^{-11}$ C^{-1} m^3, $F_{12} = 0.67 \times 10^{-11}$ C^{-1} m^3, and $F_{44} = 0.85 \times 10^{-11}$ C^{-1} m^3, deformation potential $\Xi_{ij}^p = 21$ eV, and $T = 293$ K. Red dashed profiles are calculated without flexoelectric coupling ($F_{ij} = 0$).
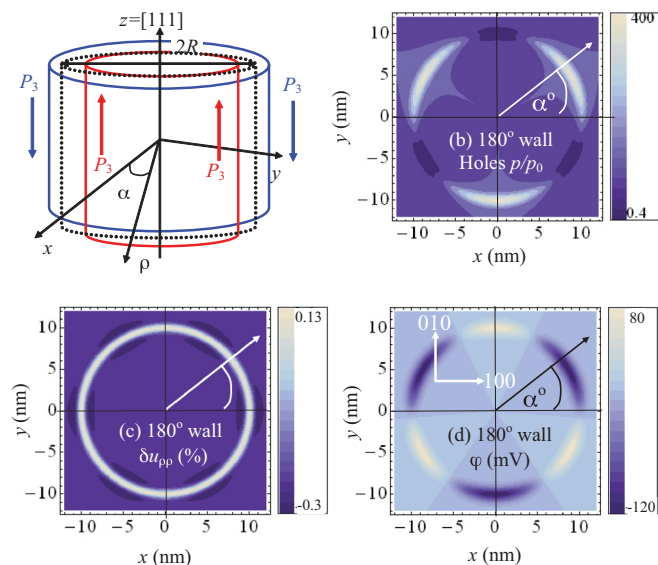
FIG. 6. (Color online) (a) Schematic of the cylindrical domain. Contour maps of the holes density p/p_0 (b), elastic strain variation $\delta u_{\rho\rho}$ (c), and potential φ (d) across the cross section of 180° cylindrical domain of radius $R = 10$ nm. The cylinder axes $z \equiv \tilde{x}_3$ coincide with the [111] crystallographic direction. Parameters are the same as in Fig. 5.

in BiFeO$_3$ and studied by use of scanning probe microscopy methods, such as c-AFM and PFM.[53]

IV. CARRIERS ACCUMULATION OF THE CYLINDRICAL 180° DOMAIN WALL

Evolved analytical theory can be extended for the case of a cylindrical domain. For the case where the domain radius R is much higher than the correlation length L_c, we use the method[54] for the nonlinear LGD-type equation solution in cylindrical geometry and derive relatively simple analytical expressions for the band bending,

$$\Delta E_p(\alpha, \rho - R) \approx \Xi_{11}^p \delta u_{\rho\rho}(\alpha, \rho - R) - e\varphi(\alpha, \rho - R), \quad (11)$$

where the polar radius $\rho = \sqrt{x^2 + y^2}$ and polar angle $\alpha = \arccos(x/\rho)$ are introduced [see Fig. 6(a)]. Equation (11) predicts that the holes density, strain, and potential spatial maps have the pronounced ring feature located at radii $|\rho - R| = L_c$ as shown in Figs. 6(b)–6(d). Three bright regions on the map in Fig. 6(b) correspond to the strong accumulation of holes; three dark regions are depleted by the holes. The ring's behavior follows from the three- and six-lobe structures of the density and band bending polar plots shown in Figs. 3(c) and 3(d). Hereafter, the static conductivity $\sigma(x, y)$ is regarded as proportional to the free carrier density as $\sigma = e\mu_n n + e\mu_p p$, where mobilities $\mu_{n,p}$ are treated as constants. Thus, the bright regions on the map in Fig. 6(b) correspond to the static conductivity enhancement; while the conductivity of the dark regions is much smaller than the bulk one. Also, it is worth noting that elastic strain ring $\delta u_{\rho\rho}$ is almost homogeneous without bright and dark regions [Fig. 6(c)], while the potential ring has three dark and three bright regions, where positions are inverted with respect to the hole's density ring [Fig. 6(d)]. The ring's behavior can be explained from

the fact that potential variation contribution $e\varphi$ dominates over the strain contribution $\Xi_{11}^p \delta u_{\rho\rho}$ into the band bending, $\Delta E_p = \Xi_{11}^p \delta u_{\rho\rho} - e\varphi$.

V. SUMMARY AND OUTCOMES

Using LGD theory, the analytical treatment of the anisotropic carrier accumulation by nominally uncharged domain walls in multiferroic BiFeO$_3$ was developed. Obtained results resolve some still outstanding issues in terms of conductivity in oxide ferroelectrics. Theoretical results are in qualitative agreement with current-AFM experiments, namely that uncharged 180°, 109°, and 71° walls are indeed conducting in BiFeO$_3$.

The modeling results for anisotropic conductance around cylindrical or ring-type domain structures is also in good agreement with recent experimental investigations,[53] where anisotropic conductance was found around a ring domain structure and attributed to polarization discontinuities and associated migration of free carriers in the material to compensate the bound charge. Though the conductivity was found to be larger in the highly charged regions, significant conductivity could also be found in areas where the bound charge should have been close to zero.

Furthermore, it is now possible to explain some inconsistencies in the reported experimental data on this topic. For instance, the reported conductivity of 71° domain walls by Farokhipoor et al.[14] in very thin BFO films can be reconciled by the fact that substrate-induced strain effects are likely larger in those films and, therefore, can lead to significant conductivity through mechanisms outlined above. In contrast, thicker films with less dense domain structures show low conductivity at 71° walls[11,53] presumably due to reduced contributions to conductivity that arise from the secondary strain-related effects.

The results presented here highlight that the effects of the angle-dependent electrostriction tensor and flexoelectric coupling-induced polarization cannot be neglected and cause real, measurable increases to the static conductivity of domain walls in ferroelectrics. Last, these studies suggest that modulation of conduction by writing circular domains should be possible in a wide variety of standard ferroelectrics, where charged domain walls are generally unstable due to high electrostatic energy cost, thus expanding the suite of materials for domain wall-based nanoelectronic applications.

*sergei2@ornl.gov

†eugene.a.eliseev@gmail.com

[1] N. D. Mermin, Rev. Mod. Phys. **51**, 591 (1979).

[2] M. Mostovoy, Phys. Rev. Lett. **96**, 067601 (2006).

[3] J. Pívratská and V. Janovec, Ferroelectrics **204**, 321 (1997).

[4] Maxim Mostovoy, Kentaro Nomura, and Naoto Nagaosa, Phys. Rev. Lett. **106**, 047204 (2011).

[5] Juan Salafranca, Rong Yu, and Elbio Dagotto, Phys. Rev. B **81**, 245122 (2010).

[6] G. Catalan, A. Lubk, A. H. G. Vlooswijk, E. Snoeck, C. Magen, A. Janssens, G. Rispens, G. Rijnders, D. H. A. Blank, and B. Noheda, Nat. Mater. **10**, 963 (2011)

[7] A. Tselev, Vincent Meunier, Evgheni Strelcov, William A. Shelton, Igor A. Luk'yanchuk, Keith Jones, Roger Proksch, Andrei Kolmakov, and Sergei V. Kalinin, ACS Nano **4**, 4412 (2010).

[8] D. Meier, J. Seidel, A. Cano, K. Delaney, Y. Kumagai, M. Mostovoy, N. A. Spaldin, R. Ramesh, and M. Fiebig, Nat. Mater. **11**, 284 (2012).

[9] W. Wu, Y. Horibe, N. Lee, S.-W. Cheong, and J. R. Guest, Phys. Rev. Lett. **108**, 077203 (2012).

[10] B. M. Vul, G. M. Guroa, and I. I. Ivanchik, Ferroelectrics **6**, 29 (1973).

[11] J. Seidel, L. W. Martin, Q. He, Q. Zhan, Y.-H. Chu, A. Rother, M. E. Hawkridge, P. Maksymovych, P. Yu, M. Gajek, N. Balke, S. V. Kalinin, S. Gemming, F. Wang, G. Catalan, J. F. Scott, N. A. Spaldin, J. Orenstein, and R. Ramesh, Nat. Mater. **8**, 229 (2009).

[12] J. Seidel, P. Maksymovych, Y. Batra, A. Katan, S.-Y. Yang, Q. He, A. P. Baddorf, S. V. Kalinin, C.-H. Yang, J.-C. Yang, Y.-H. Chu, E. K. H. Salje, H. Wormeester, M. Salmeron, and R. Ramesh, Phys. Rev. Lett. **105**, 197603 (2010).

[13] Nina Balke, Benjamin Winchester, Wei Ren, Ying Hao Chu, Anna N. Morozovska, Eugene A. Eliseev, Mark Huijben, Rama K. Vasudevan, Petro Maksymovych, Jason Britson, Stephen Jesse, Igor Kornev, Ramamoorthy Ramesh, Laurent Bellaiche, Long Qing Chen, and Sergei V. Kalinin, Nat. Phys. **8**, 81 (2012).

[14] S. Farokhipoor and B. Noheda, Phys. Rev. Lett. **107**, 127601 (2011).

[15] G. Catalan and J. F. Scott, Adv. Mater. **21**, 2463 (2009).

[16] G. Catalan, J. Seidel, R. Ramesh, and J. F. Scott, Rev. Mod. Phys. **84**, 119 (2012).

[17] Y.-H. Chu, Qian Zhan, Lane W. Martin, Maria P. Cruz, Pei-Ling Yang, Gary W. Pabst, Florin Zavaliche, Seung-Yeul Yang, Jing-Xian Zhang, Long-Qing Chen, Darrell G. Schlom, I.-Nan Lin, Tai-Bor Wu, and Ramamoorthy Ramesh, Adv. Mater. **18**, 2307 (2006).

[18] A. K. Tagantsev, L. E. Cross, and J. Fousek, *Domains in Ferroic Crystals and Thin Films* (Springer, Dordrecht, 2010).

[19] J. Wang, J. B. Neaton, H. Zheng, V. Nagarajan, S. B. Ogale, B. Liu, D. Viehland, V. Vaithyanathan, D. G. Schlom, U. V. Waghmare, N. A. Spaldin, K. M. Rabe, M. Wuttig, and R. Ramesh, Science **299**, 1719 (2003).

[20] S. Prosandeev, Igor A. Kornev, and L. Bellaiche, Phys. Rev. Lett. **107**, 117602 (2011).

[21] Axel Lubk, S. Gemming, and N. A. Spaldin, Phys. Rev. B **80**, 104110 (2009).

[22] J. X. Zhang, Y. L. Li, Y. Wang, Z. K. Liu, L. Q. Chen, Y. H. Chu, F. Zavaliche, and R. Ramesh, J. Appl. Phys. **101**, 114105 (2007).

[23] G. I. Guro, I. I. Ivanchik, and N. F. Kovtoniuk, Sov. Sol. St. Phys. **11**, 1956 (1969).

[24] M. Y. Gureev, A. K. Tagantsev, and N. Setter, Phys. Rev. B **83**, 184104 (2011).

[25] E. A. Eliseev, A. N. Morozovska, G. S. Svechnikov, Venkatraman Gopalan, and V. Ya. Shur, Phys. Rev. B **83**, 235313 (2011).

[26] E. A. Eliseev, A. N. Morozovska, G. S. Svechnikov, Peter Maksymovych, and S. V. Kalinin, Phys. Rev. B. **85**, 045312 (2012).

[27] E. A. Eliseev, A. N. Morozovska, A. Y. Borisevich, Yijia Gu, Long-Qing Chen and Venkatraman Gopalan, and S. V. Kalinin, arxiv:1204.6711.

[28] Jill Guyonnet, Iaroslav Gaponenko, Stefano Gariglio, and Patrycja Paruch, Adv. Mater. **23**, 5377 (2011).

[29] P. Maksymovych, A. N. Morozovska, P. Yu, E. A. Eliseev, Y. H. Chu, R. Ramesh, A. P. Baddorf, and S. V. Kalinin, Nano Lett. **12**, 209 (2012).

[30] V. Ya. Shur, A. V. Ievlev, E. V. Nikolaeva, E. I. Shishkin, and M. M. Neradovskiy, J. Appl. Phys. **110**, 052017 (2011).

[31] J. Hlinka and P. Márton, Phys. Rev. B **74**, 104104 (2006).

[32] A. K. Tagantsev and G. Gerra, J. Appl. Phys. **100**, 051607 (2006).

[33] G. A. Korn and T. M. Korn, *Mathematical Handbook for Scientists and Engineers* (McGraw-Hill, New York, 1961).

[34] See Supplemental Material at http://link.aps.org/supplemental/10.1103/PhysRevB.86.085315 for details of calculations.

[35] All terms proportional to the second powers of the flexoelectric coupling coefficients and their derivatives were omitted.

[36] P. Yudin, A. K. Tagantsev *et al.*, arXiv:1207.5507.

[37] P. Marton, I. Rychetsky, and J. Hlinka, Phys. Rev. B **81**, 144125 (2010).

[38] Rakesh K. Behera, Chan-Woo Lee, Donghwa Lee, Anna N. Morozovska, Susan B. Sinnott, Aravind Asthagiri, Venkatraman Gopalan, and Simon R. Phillpot, J. Phys.: Condens. Matter **23**, 175902 (2011).

[39] C. Herring and E. Vogh, Phys. Rev. **101**, 944 (1956).

[40] J. M. Ziman, *Principles of the Theory of Solids* (Cambridge University Press, Cambridge, UK, 1972), Chap. 14.

[41] D. D. Nolte, W. Walukiewicz, and E. E. Haller, Phys. Rev. Lett. **59**, 501 (1987).

[42] J. Liu, D. D. Cannon, K. Wada, Y. Ishikawa, D. T. Danielson, S. Jongthammanurak, J. Michel, and L. C. Kimerling, Phys. Rev. B **70**, 155309 (2004).

[43] Y. Sun, S. E. Thompson, and T. Nishida, J. Appl. Phys. **101**, 104503 (2007).

[44] A. N. Morozovska, E. A. Eliseev, A. K. Tagantsev, S. L. Bravina, Long-Qing Chen, and S. V. Kalinin, Phys. Rev. B **83**, 195313 (2011).

[45] G. L. Bir and G. E. Pikus, *Symmetry and Strain-induced Effects in Semiconductors* (Wiley/Halsted Press, New York, 1974).

[46] M. Dawber, K. M. Rabe, and J. F. Scott, Rev. Mod. Phys. **77**, 1083 (2005).

[47] Z. Fu, Z. G. Yin, N. F. Chen, X. W. Zhang, H. Zhang, Y. M. Bai, and J. L. Wu, Phys. Status Solidi RRL **6**, 37 (2012)

[48] Robert F. Berger, Craig J. Fennie, and J. B. Neaton, Phys. Rev. Lett. **107**, 146804 (2011)

[49] P. Zubko, G. Catalan, P. R. L. Welche, A. Buckley, and J. F. Scott, Phys. Rev. Lett. **99**, 167601 (2007).

[50]I. Ponomareva, A. K. Tagantsev, and L. Bellaiche, Phys. Rev. B **85**, 104101 (2012).

[51]W. Ma and L. E. Cross, Appl. Phys. Lett. **86**, 072905 (2005).

[52]Sh. M. Kogan, Sov. Phys. Solid State **5**, 2069 (1964).

[53]R. K. Vasudevan, A. N. Morozovska, E. A. Eliseev, J. Britson, J.-C. Yang, Y.-H. Chu, P. Maksymovych, L. Q. Chen, V. Nagarajan, and S. V. Kalinin (submitted to NanoLetters).

[54]R. K. Dodd, J. C. Eilbeck, J. D. Gibbon, and H. C. Morris, *Solitons and Nonlinear Wave Equations* (Academic Press, London, 1984).